RESEARCH ARTICLE | JULY 10 2026

Sunlight driven photocatalytic activity of Cu_2O–ZnO hetero-photocatalyst for the degradation of methylene blue: A combined experimental and theoretical study

Md. Amran Hossen Suvo ; Md. Jahidul Islam; Md. Tareq Mahmud; Md. Sabid Hossain; Mahabub Alam Bhuiyan

AIP Advances 16, 075209 (2026)
https://doi.org/10.1063/5.0341530

Sunlight driven photocatalytic activity of Cu_2O–ZnO hetero-photocatalyst for the degradation of methylene blue: A combined experimental and theoretical study

Cite as: AIP Advances 16, 075209 (2026); doi: 10.1063/5.0341530
Submitted: 2 May 2026 • Accepted: 29 June 2026 •
Published Online: 10 July 2026

Md. Amran Hossen Suvo,[1,2,3] Md. Jahidul Islam,[4] Md. Tareq Mahmud,[1] Md. Sabid Hossain,[1] and Mahabub Alam Bhuiyan[1,2,a)]

AFFILIATIONS

[1] Department of Physics, University of Dhaka, Dhaka 1000, Bangladesh
[2] Semiconductor Technology Research Centre, University of Dhaka, Dhaka 1000, Bangladesh
[3] Department of Physics, University of California, Merced, 5200 N. Lake Road, Merced, California 95343, USA
[4] Department of Materials and Metallurgical Engineering, Dhaka University of Engineering and Technology (DUET), Gazipur 1707, Bangladesh

[a)] **Author to whom correspondence should be addressed:** mahabub@du.ac.bd

ABSTRACT

ZnO, Cu_2O, and p-type Cu_2O/n-type ZnO hetero-photocatalysts were prepared at low cost with high yield by using a one-step hydrothermal method. X-ray diffraction confirmed the successful synthesis of hexagonal wurtzite ZnO and cubic phase Cu_2O crystal structures, while Fourier transform infrared spectroscopy affirmed the coexistence of both oxides in the Cu_2O–ZnO heterogeneous photocatalyst. Transmission electron microscopy revealed different sizes of ZnO nanoparticles stuck to spherical Cu_2O particles, establishing well-defined heterojunction interfaces. Optical studies showed bandgap energies of 3.12 eV for ZnO and 2.0 eV for Cu_2O, whereas the Cu_2O–ZnO heterostructure exhibited a reduced bandgap of 2.46 eV with enhanced visible-light absorption. Density functional theory calculations supported a direct-to-indirect bandgap transition with a reduction in the optical bandgap and confirmed efficient charge separation at the heterointerface. Under optimal conditions (pH ~7 and catalyst dosage of 30 mg/l), both ZnO and Cu_2O catalysts show ~45% photocatalytic degradation efficiency in 110 min of sunlight exposure in degrading methylene blue (MB) dye, whereas the Cu_2O–ZnO hetero-photocatalyst achieved ~98.08% degradation. The improved photocatalytic degradation efficiency (98.08%) of our best sample (Cu_2O–ZnO hetero-photocatalyst) was attributed to synergistic interfacial charge transfer, as validated by experimental and theoretical analyses. The effects of MB concentration (30, 40, 50, and 60 ppm) and Cu_2O–ZnO hetero-photocatalyst dosage (20, 30, and 40 mg/l) were also studied. The Cu_2O–ZnO catalyst retained at 89.73% efficiency after six cycles, demonstrating excellent stability and reusability. These combined studies might help realize the potential application of Cu_2O–ZnO catalysts as efficient sunlight-driven photocatalysts for the purification of wastewater.

I. INTRODUCTION

As a result of the industrial revolution and anthropogenic activities, water pollution is increasing day by day.[1,2] Organic, inorganic, and biological effluents are the most responsible pollutants for water pollution.[3] For example, every year, more than 800 000 tons of organic dyes are consumed around the globe, among which around 20% are discharged as wastewater during the industrial dyeing process.[4] These organic dyes are carcinogenic and mutagenic but possess highly complex molecular structural groups, making them non-biodegradable and life-threatening for human and aquatic creatures, if discharged in water without proper treatment. Methylene blue (MB), one of the most commonly consumed dyes in the dyeing and printing industries, has multiple uses.[5] Nevertheless, its

importance, the presence of stable aromatic rings in the molecular structure of MB, and its high solubility in water have made this persistence in untreated water and can cause serious consequences to humans, other mammals, fish, and can cause destruction for the ecosystem. Numerous techniques such as filtration,[6] coagulation,[7] ion-flocculation,[8] adsorption–biosorption,[9] distillation,[10] and phytoremediation[11] have been reported so far for the degradation of MB. However, these methods have their own drawbacks and limitations in terms of efficiency, cost, and secondary environmental issues.[12] At this point, the development of advanced oxidation processes (AOPs), particularly the photocatalysis, has come to the rescue and has currently gained greater attention from researchers for the degradation of toxic organic compounds such as MB and waste water treatment due to its cost-effectiveness and environment friendly approaches.[13] In this process, some metal oxide semiconductors and transition metal chalcogenide nanomaterials, such as TiO_2, ZnO, CeO_2, $BiVO_4$, CuO, Cu_2O, WO_3, ZnS, CdS, metal–organic frameworks, and carbon-based materials, are given the highest priority to be used as photocatalysts.[14–22] Among the reported materials, ZnO has gained much attention due to its strong oxidizing capability, high photosensitivity, non-toxicity, availability, low cost, and capability to quickly decompose organic molecules.[23,24] Nevertheless, having these unique physicochemical properties, the wide bandgap (3.2 eV) of ZnO nanoparticles (NPs) has diminished its potential application for the photocatalytic degradation of pollutants under sunlight irradiation since our solar spectra contain only ~5% of UV light, which can generate photo electron and hole pairs in ZnO NPs.[25–27] Furthermore, another factor, the lifetime of the photogenerated e^-–h^+ pairs, which determines the performance of the photocatalyst, is very small in case of ZnO due to the faster recombination of them.[28] In order to make ZnO NPs a sunlight-driven photocatalyst and to extend the lifetime of the photogenerated charge carriers by suppressing the recombination, numerous methods have been tested, such as doping with non-metals, transition metals, and co-doping.[29] Another efficient and convenient approach that has gained attraction is to integrate ZnO NPs with narrow bandgap semiconductors to form hybrid heterojunctions.[30] Several ZnO-based hybrid heterogeneous photocatalysts, such as ZnO/MoO_3,[31] ZnO/TiO_2,[32] ZnO/V_2O_5,[33] ZnO/CuO,[34] ZnO/NiO,[35] ZnO/CdS,[36] ZnO/ZnSe,[37] have been studied and demonstrated improved photocatalytic performance.

Meanwhile, cuprous oxide (Cu_2O), a p-type narrow bandgap (2.0–2.2 eV) semiconducting material, demonstrates strong visible light absorption and exhibits high theoretical photoelectric conversion efficiency, which have made it a good choice for visible light driven photocatalysis.[38] Despite these beneficial properties, Cu_2O suffers from high charge carrier recombination within microseconds and photo-corrosion, which lead to low photocatalytic performance while using this pristine Cu_2O as a photocatalyst.[38] Recently, a series of beneficial studies have been carried out to improve the photocatalytic performance of Cu_2O. For instance, Nie *et al.* demonstrated that doping of halogen (Cl) and metallic (Cr) elements reconstructs the energy bands of the hydrothermally synthesized Cl–Cu_2O and Cr–Cu_2O crystallites and exhibits excellent photocatalytic performance in levofloxacin removal from waste water.[39,40] Yu *et al.* prepared an Ag-doped Cu_2O thin film via electrochemical deposition and observed enhanced photocatalytic degradation of MB under sunlight irradiation.[41] Liu *et al.* created oxygen vacancies in hydrothermally grown Cu_2O by Sn ion doping, which boosted its photocatalytic performance in norfloxacin degradation.[42] In addition to these non-metallic and metallic doping into Cu_2O, several Cu_2O-based hybrid heterojunction photocatalysts, such as α-Fe_2O_3/Cu_2O,[43] Cl–Cu_2O/PANI/BC,[44] $Cu_2O/PbWO_4$,[45] CeO_2/Cu_2O,[46] $SrTiO_3$/BiOBr/Cu_2O,[47] Cu_2O/TiO_2,[48] have been fabricated recently. These newly developed Cu_2O-based heterojunction photocatalysts demonstrated excellent performance in photocatalytic degradation of complex drugs such as levofloxacin, oxytetracycline, doxycycline, sulfadiazine, and organic Rhodamine B (RhB) dye from environmental waste water.

It is evident from the above-reported literature that several systematic efforts have been made either on ZnO-based heterojunction or on Cu_2O-based heterojunction photocatalysts. Owing to the individual excellent properties of n-type ZnO and p-type Cu_2O NPs, integrating these particular two metal oxides (ZnO and Cu_2O) to form a Cu_2O–ZnO hybrid heterogeneous photocatalyst at different energy levels is thought to be beneficial and advantageous for the photocatalytic degradation of complex molecules. For instance, coupling ZnO with Cu_2O can form a p–n heterojunction effectively. Cu_2O, a p-type semiconductor with a narrow bandgap (2.0–2.2 eV), can absorb visible light efficiently and extend the photo-response of the composite into the visible region.[49] When Cu_2O and ZnO form a p–n heterojunction, the internal electric field at their interface can promote efficient charge separation by driving photo-generated electrons toward the n-type ZnO and holes toward the p-type Cu_2O. This spatial separation can suppress recombination and enhance the lifetime of charge carriers, resulting in improved photocatalytic performance under sunlight.[50] Thus, the Cu_2O–ZnO heterostructure synergistically can combine the visible light activity of Cu_2O with the stability and high electron mobility of ZnO, making it a promising system for efficient solar-driven photocatalysis.

However, only a few studies have been reported on Cu_2O–ZnO heterogeneous photocatalysts. For example, Yu *et al.* prepared p-Cu_2O/n-ZnO heterojunction thin films and showed photocatalytic degradation of norfloxacin.[38] Zou *et al.* reported the fabrication of Cu_2O–ZnO hetero-nanorod arrays on an ITO glass substrate by a two-step chemical method and showed its visible light driven photocatalytic activity for the degradation of methyl orange (MO).[51] Both of these studies were on Cu_2O–ZnO thin film based heterojunction photocatalysts, which require a special kind of experimental setup for synthesis. In another work, Wang *et al.* synthesized a Cu_2O–ZnO heterojunction by precipitation and a heat treatment process and found that this heterojunction can degrade 98% methyl orange (MO) under visible light irradiation.[52] Gaim *et al.* prepared an N-doped Cu_2O–ZnO heterojunction and employed it to degrade methyl red (MR) in the presence of solar light.[25] These studies demonstrated excellent photocatalytic performance; however, synthesis of the Cu_2O–ZnO heterojunction took place at an elevated temperature with low yield. Cheng *et al.* fabricated a Cu_2O–ZnO heterojunction with the aid of Au deposition and studied facet-dependent photocatalytic degradation of MO under visible light irradiation.[53] Wang *et al.* fabricated ZnO–Cu_2O heterojunction by a facile self-templating method and demonstrated remarkable photocatalytic degradation of Rhodamine B (RhB) dye under visible light illumination.[30] As can be seen from the reported literature, these studies require special experimental setup/higher reaction

temperature as the synthesis procedures are expensive compared to the photocatalyst yield. Furthermore, all of these studies focused on the experimental findings on the improvement of physicochemical and optical properties of the Cu_2O–ZnO heterojunction and thereafter their application for enhanced photocatalytic performance.

Considering the potential application of the Cu_2O–ZnO heterojunction for waste water treatment, a combined experimental and theoretical investigation is indispensable to realize the formation of the heterojunction and thereby the charge separation process at the Cu_2O–ZnO interfaces. However, to the best of our knowledge, only few combined efforts have been reported in the literature so far in the case of the Cu_2O–ZnO heterojunction. For instance, Kumar *et al.* studied the photo-response of the Cu_2O–ZnO heterojunction and provided a theoretical modeling, but required a thin Ga_2O_3 buffer layer.[50] Zemzemi *et al.* studied ideal $Cu_2O(111)$/ZnO surfaces and computed band offsets/adhesion energies for model interfaces and compared their findings with experimental work.[54] Ievskaya *et al.* performed theoretical band-offset studies on Cu_2O/ZnO heterojunctions fabricated in atmospheric by atomic layer deposition.[55] However, those theoretical studies typically treated ideal/epitaxial/single-crystal rather than the realistic, polycrystalline/hydrothermal nanoparticle interfaces. In addition, as per the available literature, Cu_2O–ZnO heterojunction photocatalysts have been employed mostly for the degradation of methyl orange/Rhodamine B (RhB) dyes/norfloxacin antibiotic. Considering the presence of the most commonly used organic dye, methylene blue (MB), in waste water and the potential effectiveness of Cu_2O–ZnO heterojunction photocatalyst, detailed experimental and simulation-based studies of this realistic heterojunction photocatalyst may help realize its feasible application for the degradation of life threatening MB dye in waste water.

Therefore, a simple, low-temperature hydrothermal synthesis method for creating a Cu_2O–ZnO heterojunction photocatalyst with enhanced yield and robust interfacial coupling is reported in this work. The current work provides a more physically meaningful description of charge transfer behavior in polycrystalline heterojunction systems by bridging realistic experimental nanostructures with theoretical density functional theory (DFT)-based interfacial models built from experimentally validated features, in contrast to previously published idealized or epitaxial interface models. Furthermore, the photocatalytic activity of this heterogeneous nanomaterial is systematically assessed toward the breakdown of a widely used and ecologically persistent methylene blue (MB) dye under naturally occurring sunlight irradiation. The choice of investigating this MB dye instead of some other commonly studied dyes provides a more pragmatic assessment of wastewater treatment efficacy. In addition, this work quantitatively studies the effects of some key parameters, including dye concentration and catalyst dosage, revealing their importance in governing reaction kinetics and active species creation efficiency. Furthermore, this work reveals the formation of dominant reactive species that cause MB degradation and links to the theoretically predicted band edge positions and interfacial charge redistribution. This provides a compelling experimental–theoretical mechanistic framework that validates the suggested photocatalytic pathway. Finally, the high reusability and excellent structural stability of the catalyst highlight its practical suitability for long-term wastewater treatment applications. We believe that these findings not only advance the understanding of the practical Cu_2O–ZnO heterojunction but also offer a reliable technique for integrating theoretical modeling with actual nanomaterials to design durable and efficient sunlight-driven photocatalysts.

II. MATERIALS AND METHODS

A. Chemicals and reagents

Zinc acetate di-hydrate [$Zn(CH_3COO)_2{\cdot}2H_2O$ 98%], sodium hydroxide [NaOH 98%], copper(II) nitrate hydrate [$Cu(NO_3)_2{\cdot}2.5H_2O$ 99.99%], and ethanol [C_2H_5OH 100%] were purchased from Sigma-Aldrich, USA, and were used directly from the package without further purification. Deionized water was used for washing purposes.

B. Preparation of samples

1. Synthesis of ZnO nanoparticles

ZnO nanoparticles were synthesized using the hydrothermal method. At first, 0.1M of zinc acetate dihydrate and 0.4M of sodium hydroxide were dissolved in deionized water separately in two beakers. Then, the NaOH solution was poured into the zinc acetate solution very slowly at 75 °C under continuous magnetic stirring. The mixture was stirred for 2 h and after that shifted to a Teflon-lined autoclave. Then, the autoclave was kept in the oven at 170 °C for 8 h. After the autoclave cooled down to room temperature, the precipitate of the mixture was filtered and washed with ethanol and deionized water a few times and then dried in the oven for 12 h at 60 °C. Finally, the synthesized ZnO nanoparticles were collected by using a mortar and pestle.

2. Synthesis of Cu_2O nanoparticles

At first, 10.466 g $Cu(NO_3)_2{\cdot}2.5H_2O$ was dissolved in 30 ml of absolute ethanol. Then, the dissolved solution was poured into a Teflon-lined autoclave and left in the oven for 8 h at 170 °C. After 8 h of reaction, the autoclave was left for about an hour to cool down to room temperature. When it came back to room temperature, the obtained mixture was filtered with Whatman filter paper (125 mm, Grade-1) and washed with ethanol and deionized water a few times. The obtained clay was dried in the oven at 60 °C for 12 h. Finally, Cu_2O nanoparticles were collected by using a mortar and pestle.

3. Preparation of Cu_2O–ZnO hetero-photocatalyst

At first, 1.5M $Cu(NO_3)_2{\cdot}2.5H_2O$ and zinc acetate dehydrate solution were prepared by dissolving $Cu(NO_3)_2{\cdot}2.5H_2O$ and zinc acetate dehydrate into absolute ethanol separately in two beakers. Then, the two separate solutions were mixed under continuous stirring. The mixed solution was poured into a Teflon-lined autoclave and left in the oven for 8 h at 170 °C. After the autoclave cooled down to room temperature, the obtained mixture was filtered with filter paper and washed with ethanol and deionized water a few times. The obtained clay was dried in the oven at 60 °C for 12 h. Finally, the Cu_2O–ZnO hetero-photocatalyst was collected by using a mortar and pestle. A schematic of Cu_2O–ZnO heterogeneous photocatalyst synthesis is depicted in Fig. 1.

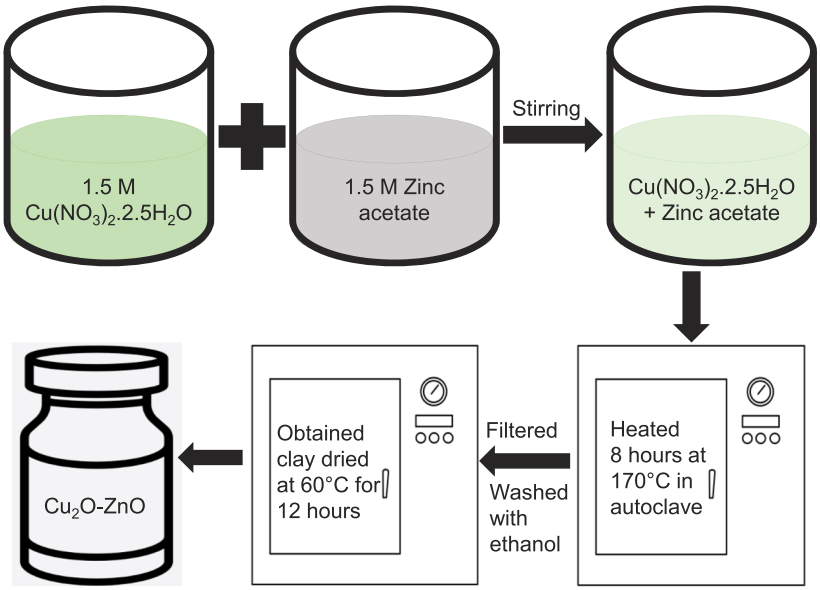

FIG. 1. Synthesis flow diagram of the Cu_2O–ZnO heterogeneous photocatalyst.

C. Sample characterization

Synthesized ZnO, Cu_2O NPs, and Cu_2O–ZnO were characterized by using numerous characterization techniques. For instance, an x-ray diffractometer (Rigaku Ultima-IV) was used to investigate the crystal structure and phase of the synthesized NPs. The measurements were carried out using Cu-K_α radiation (λ = 1.540 56 Å) operating at 40 kV and 40 mA in the Bragg–Brentano geometry. Transmission electron microscope (Talos F200X G2) equipped with a coupled camera and detector was used to study the surface morphology of the NPs at an accelerating voltage of 200 kV, providing high-resolution imaging with a point resolution of ~0.12 nm. Fourier transform infrared spectroscopy (FTIR) (IR Prestige-21) was used to study the functional groups and chemical bonds present in the NPs. UV–visible spectroscopy (Shimadzu UV-1900i) was used to study the optical properties (i.e., absorbance, optical bandgap) and to measure photocatalytic performances of the synthesized NPs.

D. Photocatalytic activity evaluation experiment

The photocatalytic activity of the synthesized Cu_2O NPs, ZnO NPs, and Cu_2O–ZnO nanocomposites was investigated on the degradation of MB dye, the most commonly used industrial dye, under the sunlight irradiation at room temperature. For this study, a 500 ml stock solution of MB dye was prepared by dissolving it in deionized water and, each time, 50 ml of the stock solution was taken for further batch experiments. An appropriate amount of the synthesized photocatalyst was added to the MB dye solution and stirred magnetically to acquire a homogeneous dispersion solution. This mixing took place for 20 min in a black box under dark conditions and was left there for the next 40 min to reach the equilibrium condition. After that, the homogeneous solution was brought under sunlight (23°43′38.6″N 90°24′05.9″E) on sunny days, and the average light intensity was 784 lux. From the exposed dispersion solution, 5 ml of solution was withdrawn using a polytetrafluoroethylene (PTFE) microporous filter and syringe system at different time intervals and poured into a spectrophotometer cuvette. The absorbance spectra (400–800 nm) of the filtered solution were acquired by using a UV–vis spectrometer (Shimadzu UV-1900i, Japan). From all of the recorded spectra corresponding to different sunlight irradiation times, the maximal absorbance values at the particular characteristic wavelength (665 nm) of MB were taken as the measured residual concentration (C_t) and used to analyze the photocatalytic degradation efficiency for respective sunlight irradiation times. All experiments were performed under identical standard conditions to allow comparison of catalyst performance. The studied solution using only the Cu_2O–ZnO photocatalyst was further analyzed by a TOC-V CPH total organic carbon (TOC) analyzer (Shimadzu, Japan) to probe the mineralization of MB by this Cu_2O–ZnO photocatalyst.

The reusability of the Cu_2O–ZnO photocatalyst was explored for up to six consecutive cycles. In this regard, the used Cu_2O–ZnO nanocomposite was recovered from the dispersion solution after each cycle of complete measurement by 5–6 min of centrifugation at 5000 rpm. Then, the retrieved nanocomposite was cleansed with ethanol and deionized water, followed by oven drying at 60 °C for 12 h, and used-retrieved in the consecutive cycles in the same way. To increase the significance of the experimental results, each of these photocatalytic experiments was carried out three times on different days and their mean values were taken along with the standard error bars.

E. Computational methodology

1. Heterointerface geometry

Cu_2O has a cubic crystal structure with a lattice parameter of 4.27 Å and a space group of *Pn3m*, as illustrated in Fig. 2(a). Among the three low-index surfaces of Cu_2O, namely, (100),

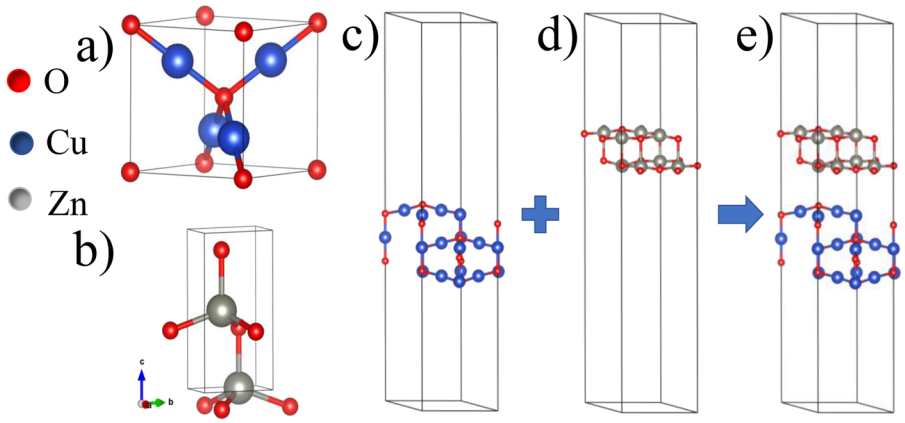

FIG. 2. (a) Unit cell of Cu_2O, (b) unit cell of ZnO, (c) (111) plane of Cu_2O with vacuum, (d) (001) plane of ZnO with vacuum, and (e) designed cell of the Cu_2O–ZnO composite.

(110), and (111), the (111) surface is the most stable.[56] To create the heterostructure, a vacuum slab with stoichiometric oxygen (O)-terminated (111) surface was formed, as shown in Fig. 2(c).

Zinc oxide (ZnO) is a semiconductor with a wide bandgap. It can be found in three different crystalline structures: hexagonal wurtzite, cubic zinc blende, or cubic rock salt. Of these three, the wurtzite structure is the most stable and is the form used in this study. Wurtzite ZnO was created by two interpenetrating hexagonal close-packed (hcp) sublattices of Zn and O. To design the composite, a vacuum slab of 2 × 2 × 1 supercell with (001) surface termination was created, as illustrated in Fig. 2(d). To design the composite, we placed two vacuum slabs 3 Å apart in the *c* direction. The vacuum thickness was set to 25 Å to prevent interaction between the periodic slabs. The lattice parameter values for the heterostructure were 6.20 Å for both *a* and *b* and 33.18 Å for *c*, resulting in a hexagonal lattice with angles of 90°, 90°, and 120°, as shown in Fig. 2(e).

The lattice mismatch was calculated by using the following equation:

$$\alpha = \left(1 - \frac{2A_{Cu_2O-ZnO(Cu,O)}}{A_{Cu_2O} + A_{ZnO}}\right) \times 100\%, \quad (1)$$

where A_{Cu_2O} and A_{ZnO} are the surface areas of pure slabs and $A_{Cu_2O-ZnO(Cu,O)}$ is the overlapping area of the composites. The calculated lattice mismatch is 2.15% for the designed composite.

2. Calculation details

The Vienna *Ab Initio* Simulation Package (VASP) code[56] was utilized for conducting first principles density functional theory (DFT) simulations. The projector-augmented wave (PAW) potentials developed in VASP were used for all atoms. This method was developed by Kresse and Joubert[57] based on Blöchl's proposal.[58] The valance electron configurations were taken as $3d^{10}$ $4s^1$ for Cu, $3d^{10}$ $4s^2$ for Zn, and $2s^2$ $2p^4$ for O. Generalized gradient approximation (GGA)[59] with the Perdew–Burke–Ernzerhof (PBE) exchange–correlation functional was employed for all of those calculations. This issue arises from traditional DFT's inability to model strongly correlated systems that exhibit significant ground-state localizations of electrons. To address this, a Hubbard U term was introduced to partially account for the over-hybridization and localization of electron orbitals. U_{eff} = 7 eV was taken for the localized electron in the Cu 3d orbital because it gave the lattice parameter value close to the experimental one, and for the case of Zn, U_{eff} = 10 eV was taken for the 3d orbitals.[60] An automatically generated gamma-centered Monkhorst–Pack scheme K-point grid was utilized, and the sampling was done by taking a 0.03 2π/Å spacing between adjacent points in reciprocal space. For the bulk Cu_2O, the k-points grid was 8 × 8 × 8; for bulk ZnO, it was 12 × 12 × 6; and for the composite, it was 6 × 6 × 1. Although VASP can perform calculations roughly at 250 eV with reliability and accuracy, we set the cutoff energy for the plane wave basis set at 520 eV for all calculations to obtain more reliable results. For geometry optimization, ionic relaxation was done until the energy variation between two iterations went below 10^{-7} eV and the force on each atom was less than 0.02 eV/Å in all three directions.

III. RESULTS AND DISCUSSION

A. Structural analysis by x-ray diffraction

To investigate the structure and phase of the synthesized NPs, an x-ray diffraction (XRD) pattern was measured for 2θ ranges from 20° to 70°. Figure 3 represents the XRD pattern of pristine ZnO, Cu_2O NPs, and Cu_2O–ZnO heterogeneous photocatalyst. In the XRD pattern of pristine ZnO, diffraction peaks appeared at 2θ = 31.74°, 34.39°, 36.24°, 47.53°, 56.57°, 62.84°, 66.39°, 67.92°,

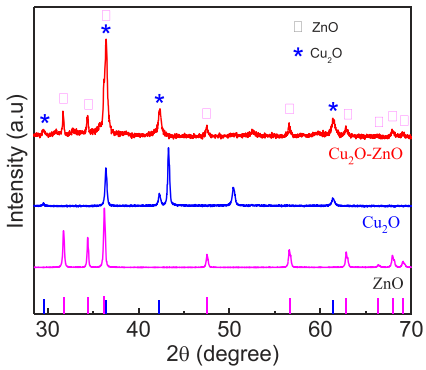

FIG. 3. X-ray diffraction patterns of ZnO, Cu_2O, and Cu_2O–ZnO nanomaterials (matched well with JCPDS card nos. 36-1451 and 05-0667 for ZnO and Cu_2O, respectively).

respectively, for the miller indices (100), (002), (101), (102), (110), (103), (112), where (101) is the characteristic peak with interplanar distance of 0.247 nm. All the diffraction peaks are exactly matched with the hexagonal wurtzite ZnO crystal structure and JCPDS card no. 36-1451.

In the XRD pattern of the pristine Cu_2O sample, the diffraction peaks appeared at $2\theta = 29.54°$, 36.40°, 42.25°, and 61.35°, corresponding to the (110), (111), (200), and (220) crystal planes of the cubic phase Cu_2O, where (200) is the characteristic peak with an interplanar distance of 0.209 nm. These diffraction peaks are closely matched with the cubic phase Cu_2O and JCPDS card no. 05-0667. Along with these characteristic reflection planes of cubic phase Cu_2O, two additional peaks have been noticed at $2\theta = 43.29°$ and 50.42°, which can be indexed to the (111) and (200) planes of a face-centered cubic metallic Cu, respectively. These findings suggest the presence of a trace amount of metallic Cu but do not alter the overall Cu_2O crystal structure.

To verify the phase composition in the Cu_2O–ZnO heterogeneous photocatalyst, a new XRD measurement was carried out after regrinding the same Cu_2O–ZnO heterogeneous sample and is presented in Fig. 3. In the repeated XRD pattern of the Cu_2O–ZnO heterogeneous sample, the diffraction peaks are observed at $2\theta = 29.54°$, 31.74°, 34.39°, 36.24°, 36.40°, 42.25°, 47.53°, 56.57°, 61.35°, 62.84°, 66.39°, 67.92°, and 69.17°. Among these, the diffraction peaks at $2\theta = 31.74°$, 34.39°, 36.24°, 47.53°, 56.57°, 62.84°, 66.39°, 67.92°, and 69.17° correspond to the (100), (002), (101), (102), (110), (103), (200), (112), and (201) crystal planes of hexagonal ZnO and matched well with the JCPDS card no. 36-1451 of ZnO and the crystal planes of the pristine ZnO sample. Meanwhile, the diffraction peaks at $2\theta = 29.54°$, 36.40°, 42.25°, and 61.35° correspond to the (110), (111), (200), and (220) crystal planes of cubic phase Cu_2O and exactly matched with the JCPDS card no. 05–0667. It is worth mentioning that no additional diffraction peaks (at $2\theta = 43.29°$ and 50.42°) have been observed like before for this Cu_2O–ZnO heterogeneous sample. Compared with the previous spectrum, the repeated XRD pattern of Cu_2O–ZnO heterogeneous sample possesses more characteristic peaks of cubic phase Cu_2O. This discrepancy is attributed to the improved homogeneity of the Cu_2O–ZnO heterogeneous sample due to the regrinding of the same sample. From these findings on the Cu_2O–ZnO heterogeneous sample, it can be stated that all the individual diffraction peaks of both ZnO and Cu_2O are present within this heterogeneous sample without any impurity. Therefore, it can be concluded that this Cu_2O–ZnO heterogeneous sample is neither hexagonal nor cubic, but rather a two-phase well crystalline nanomaterial made up of hexagonal phase ZnO and cubic phase Cu_2O.[30]

From the XRD, the average grain sizes of the synthesized nanomaterials are determined. In the case of pristine ZnO and Cu_2O, the average grain sizes are found to be 46.12 and 34.94 nm, respectively. Since the Cu_2O–ZnO heterogeneous sample is a two-phase nanomaterial, all the reflection planes of ZnO and Cu_2O noticed in the XRD of Cu_2O–ZnO are used to determine the average crystalline size of ZnO and Cu_2O, respectively, in the Cu_2O–ZnO heterogeneous sample. The obtained average crystalline sizes from these XRD data of the Cu_2O–ZnO sample are 46.12 and 25.5 nm for ZnO and Cu_2O, respectively. It is found that the average crystalline size of ZnO in the heterogeneous sample is the same as that of pristine ZnO nanomaterial. However, the average crystalline size of Cu_2O (25.5 nm) in the Cu_2O–ZnO heterogeneous sample is smaller than the average crystalline size of the pristine Cu_2O (34.94 nm) sample. The reduction in the average grain size of Cu_2O in the Cu_2O–ZnO heterogeneous nanomaterial proves the larger surface area of the catalyst.

From the XRD data, calculated average lattice parameters for pristine ZnO are a = b = 2.815 Å, c = 5.207 Å, and for pristine Cu_2O, these lattice parameters are a = b = c = 4.272 Å, which have a similarity with the corresponding JCPDS cards for hexagonal ZnO and cubic phase Cu_2O. Meanwhile, in the two-phase Cu_2O–ZnO heterogeneous nanomaterial, the average lattice parameters for hexagonal phase ZnO are a = b = 2.817 Å, c = 5.211 Å, whereas for cubic phase Cu_2O, these are a = b = c = 4.269 Å. The average full width at half maximum (FWHM) for pristine ZnO and Cu_2O is determined and found to be 0.195 and 0.254, respectively. In the case of the Cu_2O–ZnO heterogeneous sample, the average FWHM took the values 0.197 and 0.35 for ZnO and Cu_2O, respectively. The increase in the average FWHM of Cu_2O in the two-phase Cu_2O–ZnO heterogeneous nanomaterial again proves the smaller average grain size and suggests larger microstrain in Cu_2O–ZnO.

The average microstrain size for pristine ZnO and Cu_2O is 1.413×10^{-3} and 1.547×10^{-3}, respectively, whereas these average values are 1.413×10^{-3} and 2.131×10^{-3} for ZnO and Cu_2O, respectively, in the heterogeneous nanocomposite sample. This increase in the average microstrain size of Cu_2O in the Cu_2O–ZnO heterogeneous sample indicates the Cu_2O deposition with ZnO, and as a result, notable shrinkage of crystallite size happens in the heterojunction.[61] Furthermore, the average dislocation density in the case of pristine ZnO and Cu_2O is obtained as 0.000 47 and 0.000 819 nm^{-2}, respectively. This average dislocation density remains the same for ZnO in the Cu_2O–ZnO heterogeneous nanocomposite, however, it significantly increased (0.0015 nm^{-2}) for Cu_2O. This indicates an enhanced strength of the heterojunction for the study state deformation.

B. Functional group analysis by FTIR

Fourier transform infrared spectroscopy of the synthesized NPs was carried out at the wavelength of 400–4000 cm^{-1} to investigate the present functional groups and chemical bonds in those NPs. Figure 4 shows the FTIR spectra of ZnO, Cu_2O, and Cu_2O–ZnO NPs. In all three spectra, a wide absorption band at

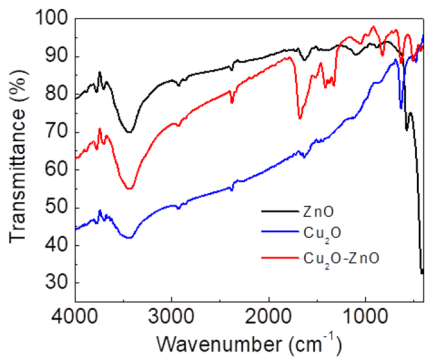

FIG. 4. Fourier transform infrared (FTIR) spectroscopy of ZnO, Cu_2O, and Cu_2O–ZnO NPs.

around 3300–3700 cm^{-1} corresponds to O–H stretching vibration of water, and two small peaks at 2924 and 2856 cm^{-1} correspond to C–H stretching vibration mode.[62] A small peak of the C=O band arrives at the wavenumber 1622 cm^{-1} for ZnO and Cu_2O, but this band arrives with a greater intensity and little shift in wavenumber (1670 cm^{-1}) for Cu_2O–ZnO heterogeneous nanomaterial.[63] A very small absorption peak at around 1480 cm^{-1} represents the carboxylate group (COO^-) in ZnO and Cu_2O but shifts very little (1512 cm^{-1}) in the case of the Cu_2O–ZnO sample.[63] In ZnO spectra, the peak at 1095 cm^{-1} corresponds to the stretching vibration of C–O attributed to zinc acetate, which is also present in Cu_2O–ZnO at 1410 cm^{-1}.[19] There is also a stretching vibration of C–C at 1049 cm^{-1} in Cu_2O–ZnO.[19] The very small peak at around 875 cm^{-1} corresponds to the bending mode of carbonate (C–O) in ZnO and Cu_2O, but this peak in Cu_2O–ZnO appeared with a higher intensity together with a slight shift in wavenumber (821 cm^{-1}), as found by other researchers.[63] In ZnO spectra, the peak at 569 cm^{-1} corresponds to the characteristic Zn–O stretching mode,[64] and in Cu_2O spectra, the peaks at 631 and 476 cm^{-1} correspond to the stretching vibration mode of Cu_2O (Cu–O).[65] These characteristic peaks are also present in the Cu_2O–ZnO spectra. The above-mentioned results affirm that the Cu_2O–ZnO heterogeneous photocatalyst is successfully synthesized, which possesses the characteristic mode of vibrations of both ZnO and Cu_2O.

C. Surface morphology study by TEM

The surface morphology of the Cu_2O–ZnO heterogeneous nanomaterial was studied by a high-resolution transmission electron microscope (HR-TEM) and is presented in Fig. 5. From the TEM image [Fig. 5(a)], it is observed that different sizes of ZnO nanoparticles are stuck to the surface of spherical shaped Cu_2O, having a size of roughly 310 nm, and a heterojunction is formed. From the HR-TEM images [Figs. 5(b) and 5(c)] of the Cu_2O and ZnO NPs, the interplanar spacing is determined and found to be 0.2463 and 0.2609 nm for Cu_2O and ZnO NPs, respectively. These determined values match the interplanar spacing of (111) crystal planes of cubic phase Cu_2O and (002) planes of hexagonal wurtzite ZnO crystals, as reported by others.[30,62,66] These morphological studies revealed that Cu_2O and ZnO NPs co-exist in the same material system and form a heterojunction.

D. Analysis of optical properties

In Fig. 6, panel (a) presents the comparability of absorbance spectra of different nano-structure samples. In the visible range, the absorbance of the ZnO (black line) sample is significantly smaller

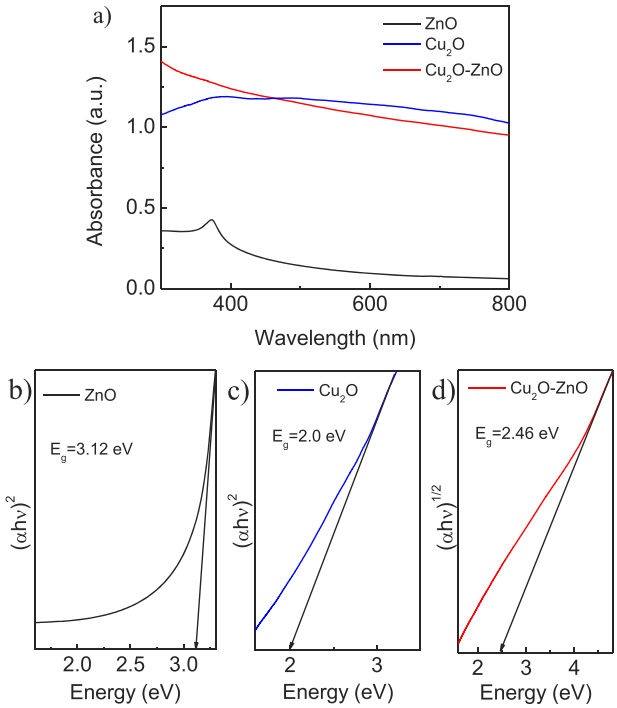

FIG. 6. (a) UV–visible absorption spectroscopy of ZnO, Cu_2O, and Cu_2O–ZnO nanophotocatalysts. Tauc plots for (b) ZnO, (c) Cu_2O, and (d) Cu_2O–ZnO nanophotocatalysts.

compared to the Cu_2O (blue line) and Cu_2O–ZnO (red line) nanostructures. The absorbances of Cu_2O and Cu_2O–ZnO almost saturate in the visible energy range. To investigate this issue, the bandgap of all the samples was calculated using the Tauc equation, $(\alpha h\vartheta) = C(h\vartheta - E_g)^{n/2}$, where E_g, h, α, C, and ϑ are the bandgap, Planck's constant, absorption coefficient, a constant, and optical frequency, respectively. The details of the bandgap energy calculations are presented in panels (b)–(d), Fig. 6. The ZnO sample shows a bandgap of 3.12 eV, and the Cu_2O sample shows a bandgap of 2.0 eV, whereas the Cu_2O–ZnO nanostructure shows a bandgap of 2.46 eV. Due to the formation of a heterojunction in the Cu_2O–ZnO nanostructure, this bandgap is higher than that of the Cu_2O nanoparticles but lower than that of the ZnO NPs. Furthermore, the photo-response is expanded throughout the UV–visible wavelength range in the case of Cu_2O–ZnO nanostructure material due to the coupling between

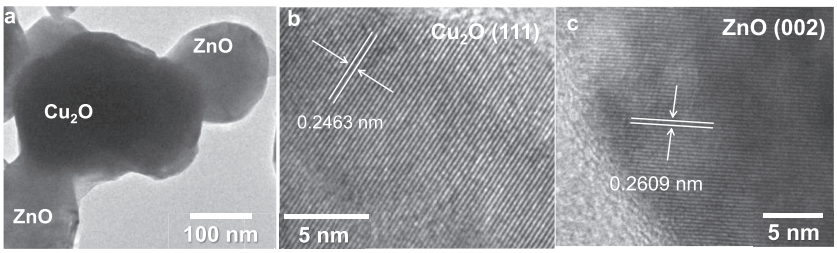

FIG. 5. (a) Transmission electron micrographs of Cu_2O–ZnO nanocomposites; HR-TEM images of (b) Cu_2O and (c) ZnO nanoparticles.

Cu_2O and ZnO. A similar result was found by Wang *et al.*[30] Therefore, it is expected that the Cu_2O–ZnO heterojunction will act as a better photocatalyst among these three nanostructures under sunlight-driven photocatalysis process.

E. Photoactivity performance

1. Effect of different catalysts on the photocatalytic degradation of MB

Figures S1–S3 show time-dependent study of the sunlight-driven photocatalytic activity of ZnO (Fig. S1), Cu_2O (Fig. S2), and Cu_2O–ZnO (Fig. S3) heterogeneous photocatalysts for the degradation of MB pollutant in Dhaka, Bangladesh (10:30 am–1:30 pm, 23°43′38.6″N 90°24′04.5″E). All the experiments were performed under identical standard conditions (natural sunlight, pH ~7, T ~33 °C, and catalyst dosage of 30 mg/l) to allow comparison of the catalysts' performance. When the photocatalysts were mixed with the MB solution, the characteristic absorption peak of MB at 665 nm decreased with sunlight irradiation time. Figure 7(a) shows the time-dependent sunlight-driven photocatalytic degradation efficiency of the ZnO, Cu_2O, and Cu_2O–ZnO nanocomposites through an analysis of the degradation of MB pollutant at this well-known characteristic absorbance peak for MB at 665 nm by using the following formula:

$$(\%)\ \text{of degradation efficiency} = \frac{C_0 - C_t}{C_0}\ \%,$$

where C_0 and C_t are the values of absorbance at time 0 and at any light irradiation time t, respectively.

Figure 7(a) demonstrates that both ZnO (black line) and Cu_2O (blue line) degrade MB at a very similar rate. Under the conditions of pH ~7, T ~33 °C, and a catalyst dosage of 30 mg/l, after 110 min of sunlight exposure, both ZnO and Cu_2O catalysts can degrade nearly 45% of the MB pollutant from the solution. The red curve in Fig. 7(a) shows the degradation efficiency of the Cu_2O–ZnO heterogeneous nano-photocatalyst. It shows that after 110 min of photo irradiation, nearly 98.08% of the MB pollutant was degraded from the solution when Cu_2O–ZnO acts as a photocatalyst, which is 2.18 times higher compared to ZnO and Cu_2O under sunlight irradiation.

Furthermore, to elucidate the degradation kinetics, we analyzed the acquired data by plotting $\ln\left(\frac{C}{C_0}\right)$ against the light exposure time for the three catalysts and present them in Fig. 7(b). It is found that the analyzed data points show an approximate linear relation between $\ln\left(\frac{C}{C_0}\right)$ and irradiation time for these catalysts. Therefore, the kinetic rate constant was determined by fitting the plotted data using the apparent first-order kinetic model: $\ln\left(\frac{C_t}{C_o}\right) = -kt$, where k implies the pseudo-first-order kinetic rate constant of the photocatalytic reaction. From the determined kinetic rate constants, we found that the degradation rate is 5.72 and 6.76 times faster in the case of the Cu_2O–ZnO heterojunction photocatalyst compared to the ZnO and Cu_2O photocatalysts, respectively.

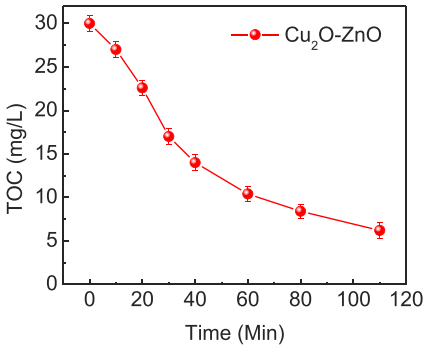

FIG. 8. Change in total organic carbon (TOC) during photodegradation of MB dye using the Cu_2O–ZnO photocatalyst under sunlight irradiation.

2. TOC analysis for the Cu_2O–ZnO heterogeneous photocatalyst

To investigate the mineralization of the MB dye, the amount of total organic carbon (TOC) in the solution during the photodegradation of MB dye using the Cu_2O–ZnO photocatalyst under sunlight irradiation was studied and presented in Fig. 8. Figure 8 shows that the TOC of the MB solution decreased regularly with light irradiation time, and after 110 min of irradiation, the TOC reduced 80.62% where MB dye degraded by 98.08% during the photodegradation process. This difference in the percentage between the photodegradation and TOC indicates that although the chromophoric structures that gave MB its distinctive blue color were successfully broken down, the dye molecules' full mineralization into inorganic species such as CO_2 and H_2O was not entirely achieved throughout the irradiation time.

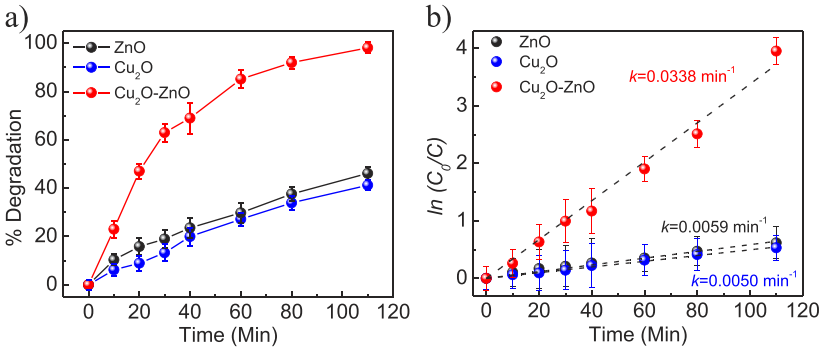

FIG. 7. Plots of (a) percentage of degradation and (b) $\ln\ (C_0/C)$ as functions of sunlight irradiation time for the degradation of MB dye with the presence of ZnO, Cu_2O, and Cu_2O–ZnO photocatalysts.

The preferential breakage of the MB molecule's chromophoric groups during the early phases of photocatalytic oxidation is responsible for the increased decolorization efficiency. The π-conjugated system and heteroatom linkages (C=N, C–S, and aromatic structures) of MB are attacked by photogenerated reactive oxygen species (ROS) under solar radiation, especially hydroxyl radicals (·OH) and superoxide anions (O_2·−), which cause rapid decolorization. However, smaller organic intermediates, including aromatic amines, sulfoxides, and low-molecular-weight carboxylic acids, are the main products of the breakdown of the chromophoric moieties. Despite not being chromophoric, these intermediates have better resistance to additional oxidative mineralization and retain significant amounts of organic carbon.

Therefore, longer irradiation times or adjustments to operational factors such as catalyst dosage, pH, and light intensity would probably be necessary for the oxidation of intermediates into CO_2 and H_2O and to achieve full mineralization. Similar patterns have been documented in earlier research on MB degradation with semiconductor photocatalysts, where the buildup of partially oxidized intermediates caused virtually total color loss to occur far earlier than full mineralization.[14,67,68]

3. Role of active radical during photocatalytic MB degradation

In the photocatalytic degradation process, the complex organic molecules are decomposed into intermediates and/or simple molecules or compounds by the reactive species. To point out the active role played by each species, the photocatalytic experiment was performed in the presence of positive hole, superoxide, hydroxyl scavengers, ammonium oxalate (AO), 1,4-benzoquinone (BQ), and tertbutyl alcohol (TBA), respectively. The degradation efficiencies in the presence of scavengers are plotted as a bar diagram along with the results found without any scavengers and can be found in Fig. 9. The comparison diagram illustrates that when BQ acts as the superoxide scavenger, only a small percentage (~10%) of efficiency is reduced. When AO acts as the positive hole scavenger, the efficiency is lowered to 67.68%, which suggests that the positive hole has a moderate effect on the photocatalysis of methylene blue by nanocomposite. Meanwhile, the hydroxyl scavenger TBA reduced the degradation efficiency of nanocomposite from 98.08% to 32%, illustrating a strong inhibiting role played in the photocatalysis. These explorations reveal that positive holes play a moderate role, whereas hydroxyl radicals play the major active role in the decomposition of complex methylene blue molecules by photocatalyst under sunlight irradiation.

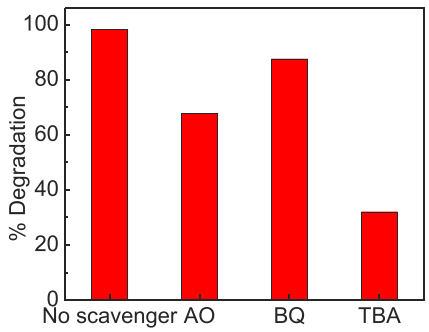

FIG. 9. Effect of different scavengers to quench the photocatalysis process.

F. Density functional theory (DFT) analysis

1. Electronic structure and density of states

To analyze the electronic characteristics of the Cu_2O–ZnO heterogeneous sample, band structure and density of states (DOS) calculations were performed, and these results are presented in Figs. 10 and 11, respectively. The band structure of Cu_2O and ZnO was also determined and shown in Figs. 10(a) and 10(b), respectively. The theoretical analysis shows that ZnO has a bandgap value of 2.37 eV while Cu_2O has a bandgap value of 0.77 eV. However, the experimental bandgap values for ZnO and Cu_2O are 3.12 and 2.0 eV, respectively. For the heterojunction, the theoretical bandgap is 0.837 eV, while the experimental value is 2.46 eV. The calculated bandgap values obtained by using the DFT method are greatly underestimated. The systematic underestimation of band gaps by PBE-type functionals is a well-known limitation since the DFT method possesses self-interaction error that leads to extreme spurious delocalization of partially occupied states and/or having Bloch semiconductor character and the lack of non-local exchange.[69,70] Despite this, PBE + U correctly captures the relative band edge positions and the electronic structure trends necessary to understand charge transfer and heterojunction formation. Moreover, our calculated bandgap values are consistent with previously reported PBE + U results for Cu_2O (0.5–0.8 eV) and ZnO (~3.22 eV) systems, confirming the reliability of our theoretical approach for qualitative interpretation.[71,72] Furthermore, the trend of the bandgap values is similar to the experimental results. Alongside, the bandgap of the Cu_2O–ZnO heterojunction is slightly higher than that of pure Cu_2O, which is consistent with the experimental findings. Therefore, the small discrepancy between the calculated and experimental band gaps does not affect the overall conclusions of this work regarding the band alignment and heterojunction formation.

The properties of the band structure can be explored by analyzing Fig. 10. It is observed that after composite formation, the conduction band minimum (CBM) remains at the gamma point, while the valence band maximum (VBM) shifts from gamma to a position between G and M. According to the elemental contribution analysis displayed in Fig. 10(f), it has been observed that only copper (Cu) and oxygen (O) are responsible for contributions in both the valence band maximum (VBM) and the conduction band minimum (CBM), and the wave functions at the CBM and VBM expressed in Figs. 10(c) and 10(d) also confirm that only the Cu_2O layer contributes at band edges.

In Fig. 11(a), it can be seen that the Cu_2O layer contributes to the formation of the valence band states near the Fermi level, which results in the composite bandgap value being closer to that of the Cu_2O bandgap. Furthermore, the orbital contribution analysis, shown in Fig. 11(b), reveals that the O-2p, Cu-3d, and Cu-4s orbitals of Cu_2O contribute toward the VBM, while the O-2s, O-2p, Cu-3d, and Cu-4s orbitals contribute toward the CBM.

2. Charge difference and interfacial analysis

In this study, we also calculated the interfacial bonding properties. Initially, the interlayer distance between two slabs was assumed

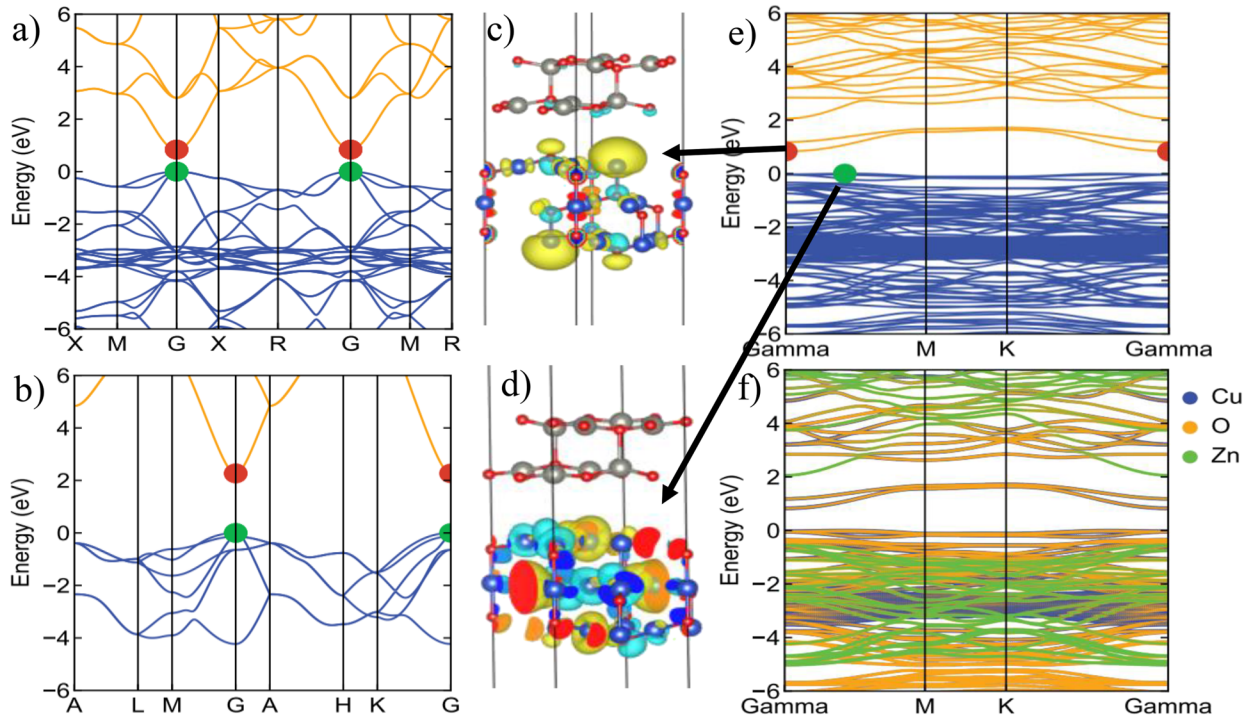

FIG. 10. Band structure of bulk (a) Cu_2O and (b) ZnO, wave function (c) at CBM and (d) at VBM, (e) band structure of composite, and (f) elemental contribution in band structure.

to be 3 Å. However, after relaxation, the distance increased to 3.43 Å, indicating that no chemical bonding was formed between the layers. The slabs were held together only by van der Waals interactions. To calculate the binding energy, we then use the following equation:

$$\text{Binding Energy, } E_b = E_{Cu_2O-ZnO} - E_{Cu_2O} - E_{ZnO}.$$

Here, in E_{Cu_2O-ZnO}, E_{Cu_2O} and E_{ZnO} represent the energy of the composite Cu_2O slab and ZnO slab, respectively. The higher the binding energy, the more force will be required to separate the slabs. In this case, the heterogeneous sample shows a binding energy of −0.131 eV, which confirms the van der Waals nature of interfacial bonding.

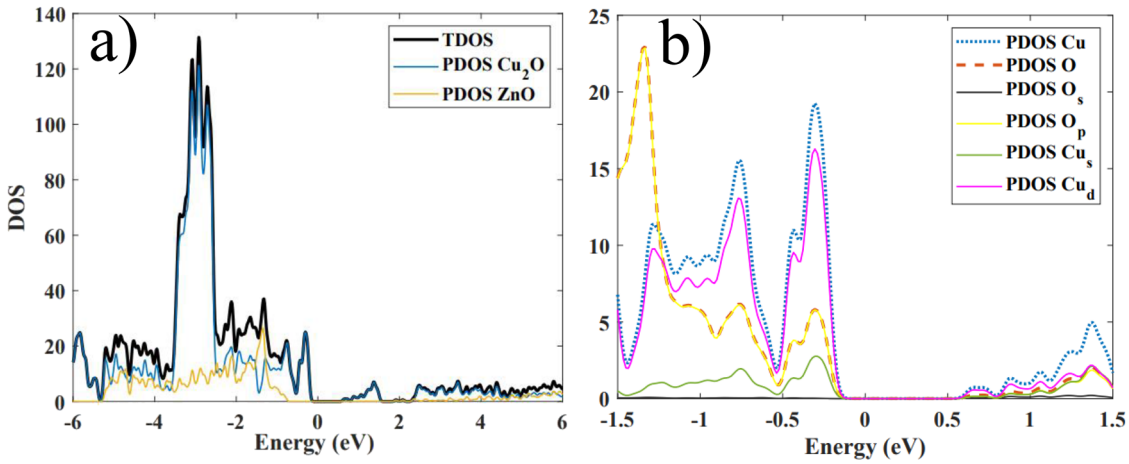

FIG. 11. (a) Total density of states (TDOS) and contribution of each slab to the DOS, and (b) elemental and orbital contribution to the DOS.

The charge density difference was calculated, shown in Fig. 12(a), using the following equation to gain insight into the electronic structure and photocatalytic activity:

$$\Delta\rho_{difference} = \rho_{total} - \sum \rho_i,$$

where $\Delta\rho_{total}$ represents the charge density of the heterogeneous sample and $\sum \rho_i$ is the summation of charge densities of fragmented Cu_2O and ZnO slabs. Figure 12(c) displays the average charge difference in the z axis, and the comparison of the linear charge difference shown in Fig. 12(c) with the planar projection of the heterostructure shown in Fig. 12(b) indicates electron transfer during the hybridization of *p*-type Cu_2O and *n*-type ZnO, confirming the formation of an internal charge separation at the heterogeneous interface of the photocatalyst. The Cu_2O surface of the interface accumulates charge, while the ZnO surface of the interface is depleted of charge. This internal polarization of the heterostructure creates S-scheme pathways for charge transfer under sunlight irradiation. This information is indispensable to comprehend and rationally design any heterogeneous photocatalyst since it plays a crucial role in separating the photogenerated electrons and holes, thereby reducing recombination and acting as an active site for redox reactions. This process ultimately leads to an increase in photocatalytic efficiency.[73]

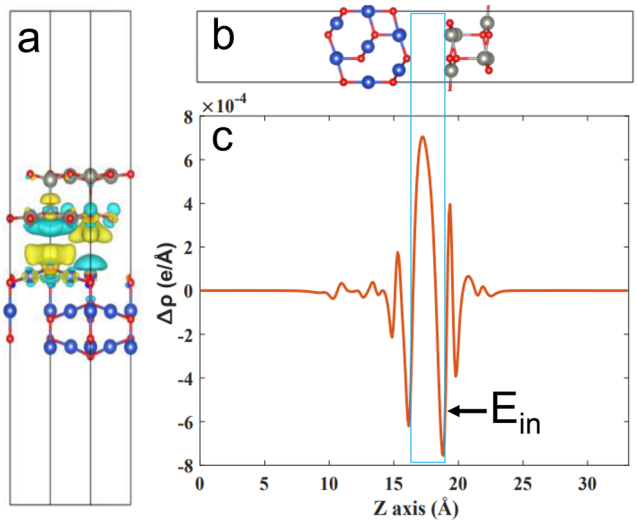

FIG. 12. (a) Charge difference, (b) designed cell of composite, and (c) planar average charge difference in the direction of the Z axis.

G. Band tuning of Cu_2O–ZnO heterostructure and the possible photodegradation mechanism

Figure 13(a) depicts a schematic diagram for the band structure tuning of Cu_2O–ZnO nanostructures. The photocatalytic performance of a semiconducting material mainly depends on its ability to generate and effectively separate photogenerated electron–hole pairs under light irradiation. The bandgap energy of the material is one of the most important parameters determining

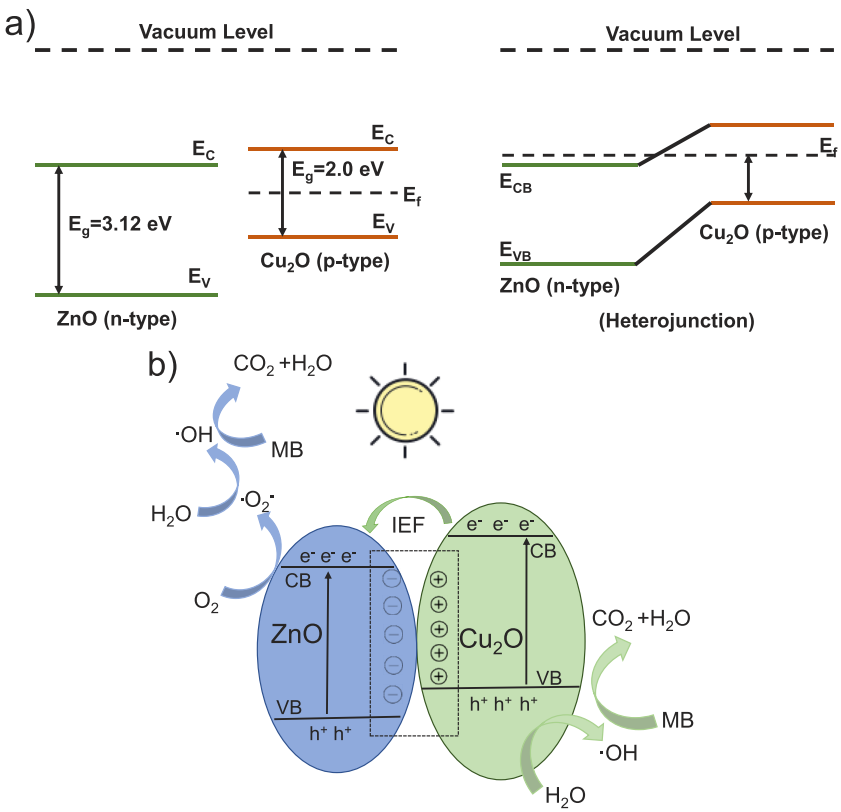

FIG. 13. (a) Tuning of the band structure of Cu_2O–ZnO heterostructure. (b) Possible mechanism for photodegradation of MB dye under sunlight irradiation in the presence of the Cu_2O–ZnO photocatalyst.

this behavior since it controls the wavelength range of light that may be absorbed as well as the efficiency of carrier excitation. By tailoring the bandgap energy of a semiconducting material, the efficiency of photon absorption and, subsequently, the separation of the photogenerated electron–hole pair can be controlled.

In our experimental setup, ZnO NPs, Cu_2O NPs, and Cu_2O–ZnO nanocomposites had estimated bandgap energies of 3.12, 2.0, and 2.46 eV, respectively. ZnO, with its wide bandgap of ~3.12 eV, can only absorb UV light, which makes up around 5% of the solar spectrum. As a result, it has comparatively less photocatalytic activity when exposed to sunlight. Cu_2O, on the other hand, has a much smaller bandgap of around 2.0 eV, which enables it to successfully absorb visible light up to wavelengths of roughly 620 nm, making use of a far greater fraction of the solar spectrum. This enhanced absorption capability of Cu_2O facilitates a higher rate of photogenerated electron–hole pair formation under sunlight irradiation.

A mixture of n-type ZnO NPs and p-type Cu_2O NPs forms a p–n heterojunction and clearly accumulates a gradient of charge carrier concentration on the junction. In the semiconductor diode analogy, the charge carriers must go from one side to the other in order to achieve equilibrium. A built-in electric field is created at the interface when n-type ZnO and p-type Cu_2O combine to produce a p–n heterojunction because of the difference in Fermi levels. As the two materials come into contact, holes drift in the opposite direction while electrons move from the higher Fermi-level n-type ZnO toward the lower Fermi-level p-type Cu_2O. This charge migration persists until equilibrium is reached, resulting in the formation of a depletion area and a potential barrier at the interface. An internal driving force is produced by this built-in potential across the junction, which promotes directional charge carrier movement and prevents recombination. The formation of such a p–n heterojunction between Cu_2O and ZnO is consistent with the recently developed S-scheme heterojunction mechanism.[74–79]

During the sunlight-driven photocatalytic process, both semiconductors absorb photons corresponding to their respective bandgaps. Because Cu_2O has a shorter bandgap, it photoexcites more readily under sunlight, generating a large number of electron–hole pairs even at lower photon energies. The photogenerated electrons in Cu_2O are easily promoted from its valence band to its conduction band. As discussed previously, the energy level of the conduction band minima (CBM) in Cu_2O is higher than that in ZnO; as a result, the photogenerated electrons from the CB of Cu_2O should be transferred to the CB of ZnO. This electron transfer is energetically favorable and significantly contributes to the spatial separation of charge carriers. Meanwhile, the negative energy photogenerated holes in Cu_2O and ZnO remain in the valence band and, therefore, increase the electron–hole lifetime by confining holes and electrons to different regions of the heterojunction.

The presence of Cu_2O with its smaller bandgap thus enhances the light-harvesting ability of the nanocomposite, enabling excitation under sunlight and increasing the overall density of charge carriers. The efficient electron migration from Cu_2O to ZnO, combined with the strong interfacial electric field, effectively reduces the recombination rate of electrons and holes. This extended lifetime of charge carriers allows for greater participation of both species in redox reactions at the photocatalyst surface. As a result, powerful radicals of reverse polarities can be produced using the well-separated electron–hole pairs. For instance, O_2 can trap electrons to form superoxide radicals $(\cdot O_2^-)$ and the holes can be trapped by water molecules to produce hydroxyl radicals (·OH). These highly reactive species can attack organic compounds such as MB and decompose their structure into simpler, harmless products.

Overall, the reduced bandgap of Cu_2O broadens the absorption range into the visible region, increases the photogenerated carrier population, and, when coupled with ZnO, facilitates efficient charge separation through the heterojunction interface. The synergistic combination of these effects accounts for the enhanced photocatalytic performance of the Cu_2O–ZnO nanocomposite. This photodegradation mechanism can be summarized by the following equation and is illustrated in Fig. 13(b):

$$Cu_2O - ZnO + \text{Sunlight} \rightarrow Cu_2O - ZnO\ (e^- + h^+),$$

$$e^- + O_2 \rightarrow \cdot O_2^- + H_2O \rightarrow \cdot OH,$$

$$h^+ + H_2O \rightarrow \cdot OH,$$

$$\cdot OH + MB \rightarrow CO_2 + H_2O.$$

H. Effect of different conditions

1. Effect of MB concentration

An important factor that affects the photocatalytic degradation performance is the concentration of the dye. The effects of MB dye

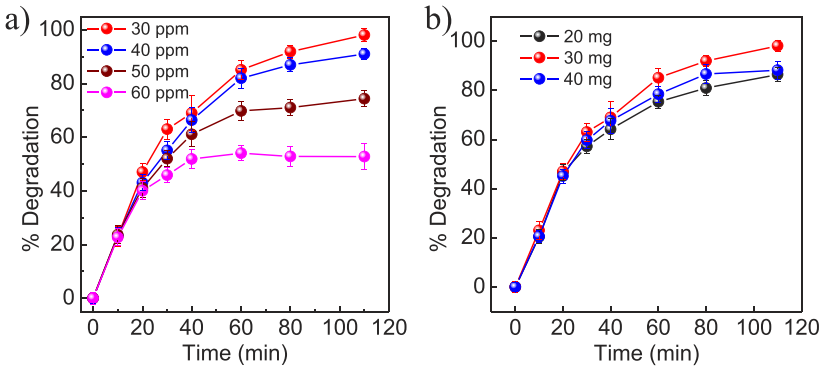

FIG. 14. (a) Effect of MB concentrations on photocatalytic degradation of MB using a fixed dose of Cu_2O–ZnO photocatalyst under sunlight irradiation. (b) Effect of Cu_2O–ZnO photocatalyst dosages on photocatalytic degradation of a fixed concentration (30 ppm) of MB dye under sunlight irradiation.

concentration on photocatalytic degradation percentage were studied for four different MB dye concentrations (30, 40, 50, and 60 ppm) with a fixed dose (30 mg/l) of Cu_2O–ZnO, and the results are represented in Fig. 14(a). From the figure, it is clearly observed that the photocatalytic degradation percentage decreases with the increase in MB dye concentration, and the highest degradation percentage was achieved for the concentration of 30 ppm of MB dye (98.08%). A possible explanation for the observed results is that increasing the dye concentration promotes the creation of larger dye aggregates, which lessens the effective contact between the dye molecules and the catalyst surface.[80] In addition, with the increasing concentration of dye at a fixed catalyst dose and fixed light irradiation, fewer photons can reach the catalyst surface as they are absorbed by the highly concentrated dye molecules, leading to a reduced degradation percentage.[80,81] So, to get the best photocatalytic degradation percentage, the optimum condition for MB dye concentration was chosen as 30 ppm and was used for all experiments.

2. Effect of Cu_2O–ZnO dosages

The effect of the catalyst dosage on the photocatalytic degradation was studied with different dosages (20, 30, and 40 mg/l) of Cu_2O–ZnO at a fixed concentration (30 ppm) of MB dye. Figure 14(b) shows the MB dye degradation percentages at different Cu_2O–ZnO heterojunction dosages. As can be observed from the graph, with the increase in dosage from 20 to 30 mg, the photocatalytic degradation percentage also increases with the irradiation time, but a further increase in dosage from 30 to 40 mg decreases the degradation percentage. After 110 min of light irradiation, the degradation percentage was observed as 86.4%, 98.08%, and 88.2% for 20, 30, and 40 mg dosages of Cu_2O–ZnO, respectively. This may happen as with the increase in catalyst dosage, photocatalytic degradation also increases by producing more active sites, but after a cutoff dosage, further increase in dosage results in decreasing degradation percentage. In this case, the possible reason of decreasing the degradation percentage for the 40 mg dosage is due to a high dosage of catalyst; irradiated light cannot penetrate through the catalyst to the dye; hence, less absorption of light by the dispersion solution happens, which leads to turbidity of the solution.[82,83] So, to get the best degradation outcome, the optimum condition of catalyst dosage was chosen as 30 mg and was used for all experiments.

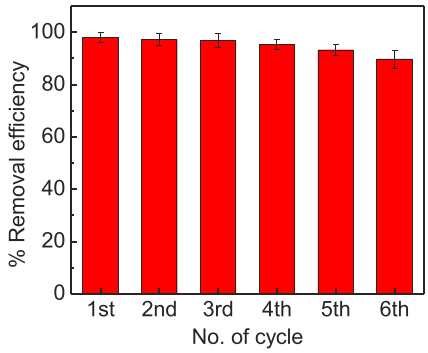

FIG. 15. Bar diagram to test the reusability of the best photocatalyst, Cu_2O–ZnO, for six consecutive cycles.

I. The recovery and reusability of the Cu_2O–ZnO photocatalyst

The reusability of the best performed catalyst, Cu_2O–ZnO heterojunction, was studied for consecutive six cycle run and the results are presented in Fig. 15. Figure 15 clearly shows that the degradation percentage remains almost same after the fourth cycle of reuse, where the degradation percentage decreases only by 4.9% after the fifth cycle and by 8.4% after the sixth cycle. This small amount of percentage dropped possibly due to the loss of catalyst during the recovery process after each cycle. The above-mentioned result suggests that Cu_2O–ZnO has a very good reusable potential and can be used for MB dye degradation for a lot of cycles.

J. A comparative analysis of MB degradation by others

Some recent studies about the photocatalytic degradation of MB dye by using different photocatalysts and light sources, along with our studies, are presented in Table I. By taking into consideration all the factors such as irradiation time, light source, and degradation efficiency, our photocatalyst performs the best photocatalytic degradation on MB dye from aqueous solution within the shortest possible time compared to any other photocatalysts studied so far for the degradation of MB dye. Therefore, it is foreseen

TABLE I. Comparative data of degradation of MB using different photocatalysts with this work.

Photocatalysts	Time (min)	Degradation (%)	Light source	References
Fe–ZnO	140	92	UV light	84
$MgFe_2O_4$	35	75	Visible light	85
$CaO.MgO.2SiO_2$	120	53	Sunlight	86
CeO_2-NPs/GO	90	90	UV-A light	87
NiO/Ag/TiO_2	60	93.1	Visible light	88
ZnO@Co-BDC	80	87.5	Visible light	89
$Zn_3(VO_4)_2$	120	87	Visible light	90
Ag@Fe_2O_3	60	97.1	UV–visible light	91
Cu_2O–ZnO	110	98.08	Sunlight	Own work

that the Cu_2O–ZnO heterogeneous photocatalyst will find practical utilization in MB dye degradation from waste water.

IV. CONCLUSIONS

In summary, ZnO NPs, Cu_2O NPs, and Cu_2O–ZnO hetero-photocatalysts were synthesized by cost-effective routes, and their structural, morphological, and optical properties were studied by numerous experimental techniques. DFT simulation shines light on the electronic properties and interfacial charge polarization of the studied samples, which validate the acquired experimental results. The Cu_2O–ZnO hetero-photocatalyst demonstrates improved photocatalytic efficiency (98.08%), compared to both ZnO (46.1%) and Cu_2O (41.2%) nano-photocatalysts under sunlight irradiation, and follows the pseudo-first-order degradation kinetic with the rate constant of 0.0338 min^{-1}. This enhanced photocatalytic performance and higher degradation rate can be attributed to the reduction in bandgap together with internal charge polarization, which facilitates the absorption of visible light and efficient photogenerated charge separation in the Cu_2O–ZnO heterojunction and thus acts as active sites for redox reaction. Our studies give valuable insights into the band alignment of two specific semiconductors, the formation of heterojunctions, and thereby the charge separation process at the Cu_2O–ZnO interfaces. Furthermore, our studies illustrate that this heterojunction-based photocatalyst can lead to a synergistic effect and can boost the photocatalytic performance under the naturally available solar light irradiation in the removal of MB dye. We believe that the knowledge gathered from both the experimental and simulation studies on this specific heterojunction-based photocatalyst will help others design and synthesize more versatile heterojunction photocatalysts using different material combinations for a wide range of environmental applications by harnessing the solar light spectrum.

SUPPLEMENTARY MATERIAL

The supplementary material contains time-dependent study of the sunlight-driven photocatalytic activity of synthesized photocatalysts for the degradation of methylene blue (MB) dye and related supporting data that complement the findings presented in the main text.

ACKNOWLEDGMENTS

We express our gratitude to the Department of Physics, University of Dhaka, Bangladesh. We are also indebted greatly to the Semiconductor Technology Research Centre of the University of Dhaka for giving us the opportunity to use the laboratory facilities rigorously throughout this research. We are grateful to the Centre for Advanced Research in Sciences of the University of Dhaka. In addition, we would like to acknowledge Dhaka University of Engineering and Technology (DUET) and Bangladesh Atomic Energy Centre, Dhaka, Bangladesh.

AUTHOR DECLARATIONS

Conflict of Interest

The authors have no conflicts to disclose.

Author Contributions

Md Amran Hossen Suvo: Data curation (lead); Formal analysis (lead); Investigation (lead); Methodology (lead); Writing – original draft (equal). **Md Jahidul Islam**: Formal analysis (equal); Software (lead); Validation (lead); Writing – original draft (equal). **Md. Tareq Mahmud**: Formal analysis (supporting); Writing – original draft (supporting); Writing – review & editing (supporting). **Md. Sabid Hossain**: Methodology (equal). **Mahabub Alam Bhuiyan**: Conceptualization (lead); Formal analysis (equal); Funding acquisition (lead); Project administration (lead); Resources (lead); Supervision (lead); Visualization (lead); Writing – original draft (equal); Writing – review & editing (lead).

DATA AVAILABILITY

The data that support the findings of this study are available from the corresponding author upon reasonable request.

REFERENCES

[1] M. Adel, M. A. Ahmed, and A. A. Mohamed, "Effective removal of indigo carmine dye from wastewaters by adsorption onto mesoporous magnesium ferrite nanoparticles," Environ. Nanotechnol., Monit. Manage. **16**, 100550 (2021).

[2] B. Lin and X. Ouyang, "Energy demand in China: Comparison of characteristics between the US and China in rapid urbanization stage," Energy Convers. Manage. **79**, 128 (2014).

[3] G. Ramalingam, N. Perumal, A. K. Priya, and S. Rajendran, "A review of graphene-based semiconductors for photocatalytic degradation of pollutants in wastewater," Chemosphere **300**, 134391 (2022).

[4] M. A. Ahmed and A. A. Mohamed, "Recent progress in semiconductor/graphene photocatalysts: Synthesis, photocatalytic applications, and challenges," RSC Adv. **13**, 421 (2023).

[5] A. Y. Goren, Y. K. Recepoğlu, Ö. Edebali, C. Sahin, M. Genisoglu, and H. E. Okten, "Electrochemical degradation of methylene blue by a flexible graphite electrode: Techno-economic evaluation," ACS Omega **7**, 32640 (2022).

[6] L. Zheng, Y. Su, L. Wang, and Z. Jiang, "Adsorption and recovery of methylene blue from aqueous solution through ultrafiltration technique," Sep. Purif. Technol. **68**, 244 (2009).

[7] Y. Y. Lau, Y. S. Wong, T. T. Teng, N. Morad, M. Rafatullah, and S. A. Ong, "Degradation of cationic and anionic dyes in coagulation-flocculation process using bi-functionalized silica hybrid with aluminum-ferric as auxiliary agent," RSC Adv. **5**, 34206 (2015).

[8] Y. N. Teixeira, F. J. de Paula Filho, V. P. Bacurau, J. M. C. Menezes, A. Zhong Fan, and R. P. F. Melo, "Removal of methylene blue from a synthetic effluent by ionic flocculation," Heliyon **8**(10), e10868 (2022).

[9] H. Li, L. Liu, J. Cui, J. Cui, F. Wang, and F. Zhang, "High-efficiency adsorption and regeneration of methylene blue and aniline onto activated carbon from waste edible fungus residue and its possible mechanism," RSC Adv. **10**, 14262 (2020).

[10] F. Banat, S. Al-Asheh, and M. Qtaishat, "Treatment of waters colored with methylene blue dye by vacuum membrane distillation," Desalination **174**, 87 (2005).

[11] M. F. Imron, S. B. Kurniawan, A. Soegianto, and F. E. Wahyudianto, "Phytoremediation of methylene blue using duckweed (*Lemna minor*)," Heliyon **5**(8), e02206 (2019).

[12] G. Crini and E. Lichtfouse, "Advantages and disadvantages of techniques used for wastewater treatment," Environ. Chem. Lett. **17**, 145 (2019).

[13] A. V. Emeline, V. K. Ryabchuk, and N. Serpone, "Photoreactions occurring on metal-oxide surfaces are not all photocatalytic: Description of criteria and conditions for processes to be photocatalytic," Catal. Today **122**, 91 (2007).

[14] R. Sultana, S. I. Liba, M. A. Rahman, N. Yeachin, I. M. Syed, and M. A. Bhuiyan, "Enhanced photocatalytic activity in RhB dye degradation by Mn and B co-doped

mixed phase TiO_2 photocatalyst under visible light irradiation," Surf. Interfaces **42**, 103302 (2023).
[15]X. Yu, J. Zhang, J. Zhang, J. Niu, J. Zhao, Y. Wei, and B. Yao, "Photocatalytic degradation of ciprofloxacin using Zn-doped Cu_2O particles: Analysis of degradation pathways and intermediates," Chem. Eng. J. **374**, 316 (2019).
[16]R. A. C. Amoresi, R. C. Oliveira, N. L. Marana, P. B. De Almeida, P. S. Prata, M. A. Zaghete, E. Longo, J. R. Sambrano, and A. Z. Simões, "CeO_2 nanoparticle morphologies and their corresponding crystalline planes for the photocatalytic degradation of organic pollutants," ACS Appl. Nano Mater. **2**, 6513 (2019).
[17]M. M. Sajid, N. Amin, N. A. Shad, S. B. khan, Y. Javed, and Z. Zhang, "Hydrothermal fabrication of monoclinic bismuth vanadate (m-$BiVO_4$) nanoparticles for photocatalytic degradation of toxic organic dyes," Mater. Sci. Eng.: B **242**, 83 (2019).
[18]D. Vaidehi, V. Bhuvaneshwari, D. Bharathi, and B. P. Sheetal, "Antibacterial and photocatalytic activity of copper oxide nanoparticles synthesized using *Solanum lycopersicum* leaf extract," Mater. Res. Express **5**, 085403 (2018).
[19]A. Kerour, S. Boudjadar, R. Bourzami, and B. Allouche, "Eco-friendly synthesis of cuprous oxide (Cu_2O) nanoparticles and improvement of their solar photocatalytic activities," J. Solid State Chem. **263**, 79 (2018).
[20]S. Kiamouche, L. Messaadia, H. Lahmar, G. Rekhila, M. Trari, and M. Benamira, "Enhanced photocatalytic degradation of Ponceau S Red dye on the novel heterosystem Fe_2O_3/WO_3 under solar light irradiation," React. Kinet., Mech. Catal. **135**, 3411 (2022).
[21]X. Zhang, J. Wang, X. X. Dong, and Y. K. Lv, "Functionalized metal-organic frameworks for photocatalytic degradation of organic pollutants in environment," Chemosphere **242**, 125144 (2020).
[22]W. Zou, B. Gao, Y. S. Ok, and L. Dong, "Integrated adsorption and photocatalytic degradation of volatile organic compounds (VOCs) using carbon-based nanocomposites: A critical review," Chemosphere **218**, 845 (2019).
[23]Y. Sun, W. Zhang, Q. Li, H. Liu, and X. Wang, "Preparations and applications of zinc oxide based photocatalytic materials," Adv. Sens. Energy Mater. **2**, 100069 (2023).
[24]N. A. F. Al-Rawashdeh, O. Allabadi, and M. T. Aljarrah, "Photocatalytic activity of graphene oxide/zinc oxide nanocomposites with embedded metal nanoparticles for the degradation of organic dyes," ACS Omega **5**, 28046 (2020).
[25]Y. T. Gaim, G. M. Tesfamariam, G. Y. Nigussie, and M. E. Ashebir, "Synthesis, characterization and photocatalytic activity of N-doped Cu_2O/ZnO nanocomposite on degradation of methyl red," J. Compos. Sci. **3**(4), 93 (2019).
[26]L. V. Bora and R. K. Mewada, "Visible/solar light active photocatalysts for organic effluent treatment: Fundamentals, mechanisms and parametric review," Renewable Sustainable Energy Rev. **76**, 1393 (2017).
[27]F. Güell, A. Galdámez-Martínez, P. R. Martínez-Alanis, A. C. Catto, L. F. da Silva, V. R. Mastelaro, G. Santana, and A. Dutt, "ZnO-based nanomaterials approach for photocatalytic and sensing applications: Recent progress and trends," Mater. Adv. **4**, 3685 (2023).
[28]Y. Yin, J. Liu, Z. Wu, T. Zhang, and Z. Li, "ZIF-8 calcination derived Cu_2O-ZnO* material for enhanced visible-light photocatalytic performance," New J. Chem. **45**, 3095 (2021).
[29]F. M. Sanakousar, C. C. Vidyasagar, V. M. Jiménez-Pérez, and K. Prakash, "Recent progress on visible-light-driven metal and non-metal doped ZnO nanostructures for photocatalytic degradation of organic pollutants," Mater. Sci. Semicond. Process. **140**, 106390 (2022).
[30]Y. Wang, J. Gao, X. Wang, L. Jin, L. Fang, M. Zhang, G. He, and Z. Sun, "Facile synthesis of core-shell ZnO/Cu_2O heterojunction with enhanced visible light-driven photocatalytic performance," J. Sol-Gel Sci. Technol. **88**, 172 (2018).
[31]A. M. Ramesh and S. Shivanna, "Hydrothermal synthesis of MoO_3/ZnO heterostructure with highly enhanced photocatalysis and their environmental interest," J. Environ. Chem. Eng. **9**, 105040 (2021).
[32]G. K. Upadhyay, J. K. Rajput, T. K. Pathak, V. Kumar, and L. P. Purohit, "Synthesis of ZnO:TiO_2 nanocomposites for photocatalyst application in visible light," Vacuum **160**, 154 (2019).
[33]R. Saravanan, V. K. Gupta, E. Mosquera, and F. Gracia, "Preparation and characterization of V_2O_5/ZnO nanocomposite system for photocatalytic application," J. Mol. Liq. **198**, 409 (2014).
[34]S. B. Endeshaw, M. Goddati, J. Lee, F. G. Aga, L. T. Tufa, and F. K. Sabir, "ZnO/CuO nanocomposites for enhanced photocatalytic and antibacterial applications: A comparative study of synthesis methods," J. Sci.: Adv. Mater. Devices **10**, 100898 (2025).
[35]Z. Chen, T. Dedova, N. Spalatu, N. Maticiuc, M. Rusu, A. Katerski, I. O. Acik, T. Unold, and M. Krunks, "ZnO/NiO heterostructures with enhanced photocatalytic activity obtained by ultrasonic spraying of a NiO shell onto ZnO nanorods," Colloids Surf., A **648**, 129366 (2022).
[36]T. R. Gurugubelli, R. V. S. S. N. Ravikumar, and R. Koutavarapu, "Enhanced photocatalytic activity of ZnO–CdS composite nanostructures towards the degradation of rhodamine B under solar light," Catalysts **12**(1), 84 (2022).
[37]S. Cho, J.-W. Jang, J. Kim, J. S. Lee, W. Choi, and K.-H. Lee, "Three-dimensional type II ZnO/ZnSe heterostructures and their visible light photocatalytic activities," Langmuir **27**, 10243 (2011).
[38]X. Yu, H. Chen, Q. Ji, Y. Chen, Y. Wei, N. Zhao, and B. Yao, "p-Cu_2O/n-ZnO heterojunction thin films with enhanced photoelectrochemical properties and photocatalytic activities for norfloxacin," Chemosphere **267**, 129285 (2021).
[39]J. Nie, X. Yu, Z. Liu, J. Zhang, Y. Ma, Y. Chen, Q. Ji, N. Zhao, and Z. Chang, "Energy band reconstruction mechanism of Cl-doped Cu_2O and photocatalytic degradation pathway for levofloxacin," J. Cleaner Prod. **363**, 132593 (2022).
[40]J. Nie, X. Yu, Z. Liu, Y. Wei, J. Zhang, N. Zhao, Z. Yu, and B. Yao, "Boosting principles for the photocatalytic performance of Cr-doped Cu_2O crystallites and mechanisms of photocatalytic oxidation for levofloxacin," Appl. Surf. Sci. **576**, 151842 (2022).
[41]X. Yu, J. Zhang, Y. Chen, Q. Ji, Y. Wei, J. Niu, Z. Yu, and B. Yao, "Ag-Cu_2O composite films with enhanced photocatalytic activities for methylene blue degradation: Analysis of the mechanism and the degradation pathways," J. Environ. Chem. Eng. **9**(5), 106161 (2021).
[42]Z. Liu, X. Yu, K. Wang, J. Zhang, and J. Niu, "Introducing oxygen cacancies to tune Cu_2O by Sn ion-doped for high-effective photocatalytic degradation of norfloxacin in wastewater," Sep. Purif. Technol. **356**, 129810 (2025).
[43]J. Nie, X. Yu, Y. Wei, Z. Liu, J. Zhang, Z. Yu, Y. Ma, and B. Yao, "Interfacial charge transfer effects of α-Fe_2O_3/Cu_2O heterojunction and enhancement mechanism of its photocatalytic oxidation," Process Saf. Environ. Prot. **170**, 241 (2023).
[44]X. Yu, Y. Tian, Y. Wei, K. Wang, Z. Liu, F. Yang, L. Chen, and J. Zhang, "Constructing p-n heterojunctions of Cl-Cu_2O and PANI on three-dimensional nanofiber networks for enhanced photocatalytic degradation of oxytetracycline," J. Alloys Compd. **1005**, 175998 (2024).
[45]X. Yu, Z. Li, Z. Liu, K. Wang, J. Zhang, and Z. Yu, "$PbWO_4$ improved the efficient photocatalytic adsorption and degradation of tetracycline and doxycycline by Cu_2O," Process Saf. Environ. Prot. **191**, 2725 (2024).
[46]Z. Liu, X. Yu, Y. Wei, K. Wang, M. Zhang, J. Liu, L. Chen, J. Zhang, and J. Niu, "Investigation of the photoelectric properties of nanostructured CeO_2/Cu_2O heterojunction: Photocatalytic degradation of sulfadiazine in water," Environ. Res. **268**, 120788 (2025).
[47]K. Wang, X. Yu, Z. Liu, Y. Wei, F. Yang, J. Zhang, J. Niu, and B. Yao, "0D/2D/0D heterostructure of $SrTiO_3$/BiOBr/Cu_2O double Z-scheme for elimination sulfadiazine: Insight into performance, mechanism, and toxicity assessment," J. Alloys Compd. **988**, 174206 (2024).
[48]T. N. Q. Trang, L. T. N. Tu, T. V. Man, M. Mathesh, N. D. Nam, and V. T. H. Thu, "A high-efficiency photoelectrochemistry of Cu_2O/TiO_2 nanotubes based composite for hydrogen evolution under sunlight," Composites, Part B **174**, 106969 (2019).
[49]Q. Su, C. Zuo, M. Liu, and X. Tai, "A review on Cu_2O-based composites in photocatalysis: Synthesis, modification, and applications," Molecules **28**(14), 5576 (2023).
[50]N. Kumar, M. Patel, M. J. Park, C. Jeong, and J. Kim, "Field-effect passivation of the Cu_2O/ZnO transparent heterojunction photovoltaic device using Ga_2O_3 thin film," ACS Appl. Energy Mater. **6**, 6496 (2023).
[51]X. Zou, H. Fan, Y. Tian, and S. Yan, "Synthesis of Cu_2O/ZnO hetero-nanorod arrays with enhanced visible light-driven photocatalytic activity," CrystEngComm **16**, 1149 (2014).
[52]X. S. Wang, Y. D. Zhang, Q. C. Wang, B. Dong, Y. J. Wang, and W. Feng, "Photocatalytic activity of Cu_2O/ZnO nanocomposite for the decomposition of

methyl orange under visible light irradiation," Sci. Eng. Compos. Mater. **26**, 104 (2019).
[53]L. Cheng, G. Wu, D. Ruan, H. Wu, and A. Liu, "Morphological guidance and proportional control of Cu_2O/ZnO core/shell heterojunction with enhanced visible-light-driven photocatalytic performance," J. Mater. Sci. **58**, 186 (2023).
[54]M. Zemzemi, S. Alaya, and Z. Ben Ayadi, "*Ab initio* study of heterojunction discontinuities in the ZnO/Cu_2O system," J. Exp. Theor. Phys. **118**, 945 (2014).
[55]Y. Ievskaya, R. L. Z. Hoye, A. Sadhanala, K. P. Musselman, and J. L. MacManus-Driscoll, "Fabrication of ZnO/Cu_2O heterojunctions in atmospheric conditions: Improved interface quality and solar cell performance," Sol. Energy Mater. Sol. Cells **135**, 43 (2015).
[56]J. Hafner and G. Kresse, "The Vienna ab-initio simulation program VASP: An efficient and versatile tool for studying the structural, dynamic, and electronic properties of materials," in *Properties of Complex Inorganic Solids* (Springer, 1997), pp. 69–82.
[57]G. Kresse and D. Joubert, "From ultrasoft pseudopotentials to the projector augmented-wave method," Phys. Rev. B **59**, 1758 (1999).
[58]P. E. Blöchl, "Projector augmented-wave method," Phys. Rev. B **50**, 17953 (1994).
[59]J. P. Perdew, K. Burke, and M. Ernzerhof, "Generalized gradient approximation made simple," Phys. Rev. Lett. **77**, 3865 (1996).
[60]A. K. Mishra, A. Roldan, and N. H. De Leeuw, "A density functional theory study of the adsorption behaviour of CO_2 on Cu_2O surfaces," J. Chem. Phys. **145**(4), 044709 (2016).
[61]H. Makhlouf, M. Weber, O. Messaoudi, S. Tingry, M. Moret, O. Briot, R. Chtoutou, and M. Bechelany, "Study of Cu_2O\ZnO nanowires heterojunction designed by combining electrodeposition and atomic layer deposition," Appl. Surf. Sci. **426**, 301 (2017).
[62]F. Ahmed, S. Kumar, N. Arshi, M. S. Anwar, B. H. Koo, and C. G. Lee, "Rapid and cost effective synthesis of ZnO nanorods using microwave irradiation technique," Funct. Mater. Lett. **4**, 1 (2011).
[63]M. J. Chithra, M. Sathya, and K. Pushpanathan, "Effect of pH on crystal size and photoluminescence property of ZnO nanoparticles prepared by chemical precipitation method," Acta Metall. Sin. **28**, 394 (2015).
[64]H. S. Wasly, M. S. A. El-Sadek, and M. Henini, "Influence of reaction time and synthesis temperature on the physical properties of ZnO nanoparticles synthesized by the hydrothermal method," Appl. Phys. A **124**, 76 (2018).
[65]M. Tahir, M. Zeb, A. Alamgeer, S. Hussain, M. R. Sarker, D. N. Khan, F. Wahab, and S. H. M. Ali, "Cuprous oxide nanoparticles: Synthesis, characterization, and their application for enhancing the humidity-sensing properties of poly(dioctylfluorene)," Polymers **14**(8), 1503 (2022).
[66]M. Mallik, S. Monia, M. Gupta, A. Ghosh, M. P. Toppo, and H. Roy, "Synthesis and characterization of Cu_2O nanoparticles," J. Alloys Compd. **829**, 154623 (2020).
[67]L. Song, T. Li, and S. Zhang, "Synthesis and characterization of Ag/$AgBrO_3$ photocatalyst with high photocatalytic activity," Mater. Chem. Phys. **182**, 119 (2016).
[68]Y. Ahmed, Z. Yaakob, and P. Akhtar, "Degradation and mineralization of methylene blue using a heterogeneous photo-Fenton catalyst under visible and solar light irradiation," Catal. Sci. Technol. **6**, 1222 (2016).
[69]B. J. Morgan, D. O. Scanlon, and G. W. Watson, "The use of the '+U' correction in describing defect states at metal oxide surfaces: Oxygen vacancies on CeO_2 and TiO_2, and Li-doping of MgO," e-J. Surf. Sci. Nanotechnol. **7**, 389 (2009).
[70]A. K. Mishra, A. Roldan, and N. H. De Leeuw, "CuO surfaces and CO_2 activation: A dispersion-corrected DFT+U study," J. Phys. Chem. C **120**, 2198 (2016).
[71]P. Makkar and N. N. Ghosh, "A review on the use of DFT for the prediction of the properties of nanomaterials," RSC Adv. **11**, 27897 (2021).
[72]S. Sharma and J. Sharma, "DFT study of electronic and optical properties of Cu_2O nanostructures," AIP Conf. Proc. **2093**, 020032 (2019).
[73]X. Liu, P. Cheng, X. Zhang, T. Shen, J. Liu, J. C. Ren, H. Wang, S. Li, and W. Liu, "Enhanced solar-to-hydrogen efficiency for photocatalytic water splitting based on a polarized heterostructure: The role of intrinsic dipoles in heterostructures," J. Mater. Chem. A **9**, 14515 (2021).
[74]M. Sayed, K. Qi, X. Wu, L. Zhang, H. García, and J. Yu, "Cu-based S-scheme photocatalysts," Chem. Soc. Rev. **54**, 4874 (2025).
[75]X. Zeng, Q. Gao, P. Song, X. Zhang, J. Xie, Q. Dong, J. Qi, X. S. Xing, and J. Du, "Integration of a Cu_2O/ZnO heterojunction and Ag@SiO_2 into a photoanode for enhanced solar water oxidation," RSC Adv. **14**, 4568 (2024).
[76]N. P. de Moraes, R. D. M. dos Santos, M. E. V. Gouvêa, A. de Siervo, R. da Silva Rocha, D. A. Reddy, Y. Lianqing, M. R. de Vasconcelos Lanza, and L. A. Rodrigues, "Solar-based photocatalytic ozonation employing novel S-scheme ZnO/Cu_2O/CuO/carbon xerogel photocatalyst: Effect of pH, salinity, turbidity, and temperature on salicylic acid degradation," Environ. Sci. Pollut. Res. **30**, 98211 (2023).
[77]S. K. Baek, S. S. Kwak, J. S. Kim, S. W. Kim, and H. K. Cho, "Binary oxide p-n heterojunction piezoelectric nanogenerators with an electrochemically deposited high p-type Cu_2O layer," ACS Appl. Mater. Interfaces **8**, 22135 (2016).
[78]J. Low, J. Yu, M. Jaroniec, S. Wageh, and A. A. Al-Ghamdi, "Heterojunction photocatalysts," Adv. Mater. **29**(20), 1601694 (2017).
[79]R. Bengas, H. Lahmar, K. M. Redha, L. Mentar, A. Azizi, G. Schmerber, and A. Dinia, "Electrochemical synthesis of n-type ZnS layers on p-Cu_2O/n-ZnO heterojunctions with different deposition temperatures," RSC Adv. **9**, 29056 (2019).
[80]I. Groeneveld, M. Kanelli, F. Ariese, and M. R. van Bommel, "Parameters that affect the photodegradation of dyes and pigments in solution and on substrate–An overview," Dyes Pigm. **210**, 110999 (2023).
[81]K. M. Reza, A. Kurny, and F. Gulshan, "Parameters affecting the photocatalytic degradation of dyes using TiO_2: A review," Appl. Water Sci. **7**, 1569 (2017).
[82]N. Soltani, E. Saion, M. Z. Hussein, M. Erfani, A. Abedini, G. Bahmanrokh, M. Navasery, and P. Vaziri, "Visible light-induced degradation of methylene blue in the presence of photocatalytic ZnS and CdS nanoparticles," Int. J. Mol. Sci. **13**, 12242 (2012).
[83]D. R. Paul, R. Sharma, S. P. Nehra, and A. Sharma, "Effect of calcination temperature, pH and catalyst loading on photodegradation efficiency of urea derived graphitic carbon nitride towards methylene blue dye solution," RSC Adv. **9**, 15381 (2019).
[84]K. A. Isai and V. S. Shrivastava, "Photocatalytic degradation of methylene blue using ZnO and 2%Fe–ZnO semiconductor nanomaterials synthesized by sol–gel method: A comparative study," SN Appl. Sci. **1**, 1247 (2019).
[85]A. F. Cabrera, C. E. Rodríguez Torres, S. G. Marchetti, and S. J. Stewart, "Degradation of methylene blue dye under dark and visible light conditions in presence of hybrid composites of nanostructured $MgFe_2O_4$ ferrites and oxygenated organic compounds," J. Environ. Chem. Eng. **8**, 104274 (2020).
[86]S. Kumar Venkatraman, M. Saraswat, R. Choudhary, F. Senatov, S. Kaloshkin, and S. Swamiappan, "Photocatalytic degradation of methylene blue dye by calcium-and magnesium-based silicate ceramics," ChemistrySelect **5**, 12198 (2020).
[87]Z. Kalaycıoğlu, B. Özuğur Uysal, Ö. Pekcan, and F. B. Erim, "Efficient photocatalytic degradation of methylene blue dye from aqueous solution with cerium oxide nanoparticles and graphene oxide-doped polyacrylamide," ACS Omega **8**, 13004 (2023).
[88]W. Mohammed, M. Matalkeh, R. M. Al Soubaihi, A. Elzatahry, and K. M. Saoud, "Visible light photocatalytic degradation of methylene blue dye and pharmaceutical wastes over ternary NiO/Ag/TiO_2 heterojunction," ACS Omega **8**, 40063 (2023).
[89]B. A. Berehe, A. A. Desalew, G. W. Derbe, D. M. Misganaw, K. S. Mohammed, J. Y. Chang, and W. M. Girma, "Enhanced photocatalytic degradation of methylene blue dye via valorization of a polyethylene terephthalate plastic waste-derived metal-organic framework-based ZnO@Co-BDC composite catalyst," Nanoscale Adv. **7**, 3834 (2025).
[90]N. Matinise, N. Botha, A. Fall, and M. Maaza, "Enhanced photocatalytic degradation of methylene blue using zinc vanadate nanomaterials with structural and electrochemical properties," Sci. Rep. **15**, 26333 (2025).
[91]V. Jadhav, Y. Dhanwate, P. Raut, S. Shinde, R. Sawant, and A. Bhagare, "Efficient photocatalytic methylene blue dye degradation from green-synthesized silver-doped iron oxide (Ag@Fe_2O_3) nanostructures," Discover Nano **20**, 66 (2025).